Author/s:
Bergemann, M;Lane, TP;Wales, S;Narsey, S;Louf, V

Title:
High-resolution simulations of tropical island thunderstorms: Does an increase in resolution improve the representation of extreme rainfall?

Date:
2022-10-14

Citation:
Bergemann, M., Lane, T. P., Wales, S., Narsey, S. & Louf, V. (2022). High-resolution simulations of tropical island thunderstorms: Does an increase in resolution improve the representation of extreme rainfall?. QUARTERLY JOURNAL OF THE ROYAL METEOROLOGICAL SOCIETY, 148 (748), https://doi.org/10.1002/qj.4360.

Persistent Link:
https://hdl.handle.net/11343/317574

Received: 9 January 2022 | Revised: 4 August 2022 | Accepted: 19 August 2022

DOI: 10.1002/qj.4360

Quarterly Journal of the Royal Meteorological Society RMetS

RESEARCH ARTICLE

High-resolution simulations of tropical island thunderstorms: Does an increase in resolution improve the representation of extreme rainfall?

Martin Bergemann[1,2,3] | **Todd P. Lane**[2,3] | **Scott Wales**[2,3,4] | **Sugata Narsey**[4] | **Valentin Louf**[3,4,5]

[1]German Climate Computing Centre (DKRZ), Hamburg, Germany

[2]School of Geography, Earth and Atmospheric Sciences, The University of Melbourne, Parkville, Victoria, Australia

[3]ARC Centre of Excellence for Climate Extremes (CLEX), Sydney, New South Wales, Australia

[4]Australian Bureau of Meteorology, Melbourne, Victoria, Australia

[5]School of Earth Atmosphere and Environment, Monash University, Clayton, Victoria, Australia

Correspondence
M. Bergemann, Deutsches Klimarechenzentrum, Bundesstraße 45a, 20146 Hamburg, Germany.
Email: bergemann@dkrz.de

Funding information
Australian Research Council, Grant/Award Number: CE170100023

Abstract

Recent increases in computational resources have led to the application of kilometre- and sub-kilometre-scale simulations in research, numerical weather prediction, and climate modelling alike. Despite anticipated improvements with resolution, there is still considerable work needed to evaluate how well such models improve the representation of intense convection. In this study we conduct ensemble simulations with kilometre- and sub-kilometre-scale horizontal grids to investigate intense convective events in the tropical island thunderstorm system Hector, which frequently occurs over the Tiwi Islands in North Australia. To avoid losing information through spatio-temporal averaging we apply a tracking algorithm to simulated and observed storms. When compared with observations, the model storms exhibit a lack of propagation across the study domain. In general, simulated storms are too intense but too small and too short-lived. This is especially true for the sub-kilometre simulations, where storms are more intense, smaller, and more numerous than in the kilometre-scale counterparts. We argue that size and duration errors compensate for storm number and intensity errors, which could lead to misleading interpretations when only comparing time and space averages of rainfall fields. Investigating some properties of the simulated storms suggests that storms with high rainfall intensities have stronger updrafts in the sub-kilometre model and are accompanied by an increase in cold pool intensity. The results and their resolution sensitivities highlight that the remaining parametrisations and their many tuning parameters in high-resolution set-ups influence the representation of convective storms in such models.

KEYWORDS

convection rainfall, mesoscale scale, observational data analysis, regional and mesoscale modelling, severe weather, Tropics

1 | INTRODUCTION

Convective storm systems in coastal areas of the Tropics, such as the Maritime Continent, are of extraordinary importance for the Earth climate system by distributing heat and momentum in the tropical atmosphere (e.g., Matsuno, 1966; Ramage, 1968; Gill, 1980; Trenberth *et al.*, 2009 and others). The geography of the Maritime Continent, with thousands of islands, plays a pivotal role in driving the tropical circulations. Yamanaka *et al.* (2018) showed that convective systems over the Maritime Continent contribute to roughly 20% of the global latent heat budget. Many of these convective systems are island thunderstorms that are strongly influenced by mesoscale land–sea interactions (Mori *et al.*, 2004; Qian, 2008; Bergemann *et al.*, 2015) and can become considerably intense (Simpson *et al.*, 1980; 1993), even if large-scale atmospheric conditions are suppressed (Bergemann and Jakob, 2016).

A well-known example of a tropical island thunderstorm is Hector, a single- or multicell storm system occurring frequently in the late afternoon to early evening over the Tiwi Islands, located in the south of the Timor Sea roughly 100 km north of Darwin, Australia (11.6° S/130.9° E). Its frequent occurrence over the Tiwi Islands' rather flat terrain during the monsoon transition season (October–December, March–April) has made Hector a focus of various field campaigns (Keenan *et al.*, 1989; 2000; May *et al.*, 2008; Vaughan *et al.*, 2008; Leroy *et al.*, 2016). Most notable are the Maritime Continent Thunderstorm Experiment (MCTEX; Keenan *et al.*, 2000), the Island Thunderstorm Experiment (Keenan *et al.*, 1989) and the Tropical Warm Pool International Cloud Experiment (May *et al.*, 2008).

Beringer *et al.* (2001) used observations from MCTEX to determine various atmospheric variables, like convective available potential energy or wind shear, to identify four different types of Hector: (1) Hector, (2) suppressed Hector, (3) no Hector, and (4) late-developing Hector. They suggested that the absence of Hector (suppressed Hector and no Hector) could be either due to previously traversing squall lines consuming the convective available potential energy (suppressed Hector) or due to an increased wind shear (no Hector). Schafer *et al.* (2001) took advantage of a comparatively dense network of sensors over the Tiwi Islands during MCTEX. These observations were used to determine horizontal winds, mean virtual potential temperature, boundary-layer depth, air temperature, and convergence. Horizontal and vertical variations of these descriptors were used to characterise the development of the boundary layer. These observations combined with numerical simulations showed that Hector is strongly influenced by the sea-breeze convergence zones propagating around the islands.

Crook (2001) combined observations from MCTEX with model simulations to show that low-level moisture and ambient wind speed and direction play an important role in modulating the intensities of the storms. Hector events tend to increase as ambient lower level wind flow decreases and the wind direction points towards the major axis of the main island. Interactions of the sea breeze with storm-associated cold pools can further modulate the occurrence, position, and intensity of the Hector events.

High-resolution convection-permitting model simulations have gained an increasing popularity for investigating Hector and other island thunderstorm events during the past years. Using large-eddy simulations with a resolution of 100 m, (Dauhut *et al.*, 2016; 2017) showed that the tallest updrafts within Hector storm systems are able to penetrate the stratosphere. The studies suggest that reduced mixing in the troposphere as well as intensification of low-level convergence lines from cold pools are crucial for the occurrence of such very deep convective systems. Zhu *et al.* (2012) used the Weather Research and Forecasting (WRF) model at 1 km horizontal resolution to simulate four Hector events and described a tendency of the model to underestimate the occurrence and intensity of such events. Focusing on convective storms over coastal South Africa, Love *et al.* (2011) investigated the simulated diurnal cycle of deep island convection using the UK Met Office's Unified Model (UM) at various horizontal resolutions of up to 4.5 km. They found that, compared with observations, convection over coastal land is triggered early in the model, leading to a too-early peak of rainfall. This is in agreement with other high-resolution model simulations using the WRF model (Gianotti *et al.*, 2011; Hassim *et al.*, 2016; Vincent and Lane, 2017).

With the rise of convection-permitting models, increasing attention has been drawn to understanding convective extreme events (e.g., Chan *et al.*, 2013; 2014; Gevorgyan, 2018). Despite the recent efforts in model development, there is no clear consensus to which degree an increase in model resolution leads to an improvement of the representation of convective extreme events in realistic scenarios. For example, Jucker *et al.* (2020) showed with the help of the UM and WRF models at both kilometre- and sub-kilometre-scale configurations that important characteristics of simulated convective systems across tropical northern Australia do not change significantly with an increase in resolution. Other rather longer-term studies using high-resolution models apply some kind of spatial or temporal averaging (Birch *et al.*, 2016; Vincent and Lane, 2017; Keat *et al.*, 2019), which also has disadvantages when investigating extreme conditions.

The frequent occurrence of the thunderstorm system Hector together with its proximity to a long-running ground-based dual-polarised research radar makes the Tiwi Islands a useful study area to investigate intense tropical convective events. This study therefore aims at investigating intense convective events over the Tiwi Islands going beyond single events while applying as little as possible averaging. This is realised by investigating consecutive Hector events using individual thunderstorm tracks from an ensemble of model simulations at different resolutions (kilometre and sub-kilometre scale). The results are then compared with ground-radar-based observations.

The article is organised as follows: Section 2.1 gives a short introduction to the study area, and Sections 2.2 and 2.3 will describe the ground-based radar dataset and the model set-up. Section 2.4 explains the algorithm that is applied to observational and model data to track thunderstorm events in space and time. Section 3 examines the modelling results and compares them with the observations, which is followed by a discussion and conclusion in Section 4.

2 | MODEL, OBSERVATIONS AND METHODS

2.1 | Study area

A rigorous investigation of intense convective events simulated in cloud-resolving models is a challenging task in various aspects. All statistics considering extreme events should be based on data with a sufficient sample size, because the appearance of extremes, depending their definition, is infrequent. This makes it necessary to run model simulations for longer time periods, which can become difficult given the computational complexity and large data output of cloud-resolving simulations. To identify a sufficiently large sample of intense convective events that can be potentially captured by a cloud-resolving model we scan radar-derived rainfall observations from a 17-year record for consecutive occurrences of strong tropical coastal thunderstorm events over the Tiwi Islands in northern Australia. This location was chosen because of the frequent occurrence of island thunderstorm systems and the availability of high-quality ground-based radar observations in this area. Located roughly 100 km north of Darwin, Australia, the Tiwi Islands form a group of 11 mostly small islands. Their terrain is rather flat, with an average height of 35 m above sea level, hills do not extent beyond 150 m (see Figure 1a for details on location and terrain). Previous studies have hypothesised that the sizes of the two main islands—Bathurst Island and Melville Island—favour the collision of two sea-breeze fronts which supports the development of deep convective storms (Crook, 2001; Saito *et al.*, 2001). Hence, the Tiwi Islands are subject to regularly occurring island thunderstorm events. We are specifically looking for events occurring during the monsoon build-up period as defined in Narsey *et al.* (2017). These periods only are considered here because convection is most distinct and strongly influenced by local forcing and less by the synoptic-scale forcing, which allows for a better comparison between different events. For our investigation we choose a sequence of eight consecutive Hector events during the monsoon build-up period from November 11 to November 19, 2006. This period is the longest sequence of successive Hector events in the entire 17-year radar archive, during monsoon build-up and break periods defined by Narsey *et al.* (2017). To identify the mentioned time period we visually scanned the C-band dual-polarisation radar (CPOL) radar-based precipitation estimates for consecutive, distinguishable rainfall events occurring over the Tiwi Islands.

2.2 | Radar-based observations

For comparing simulated rainfall with observational data we use ground-radar precipitation estimates. These estimates are based on measurements from the CPOL located at Gunn Point (12.249° S; 131.044° E), roughly 65 km south of the Tiwi Islands (Keenan *et al.*, 1998). CPOL operated at a frequency of 5.6 GHz, has an update interval of 10 min, and a maximum range of ∼150 km. The dataset recently underwent a series of calibrations, quality controls and processing, which are described in detail in Louf *et al.* (2018). The rain-rate retrieval algorithm (Thompson *et al.*, 2017) is applied to the data before interpolating from polar to Cartesian Coordinates with a resolution of 2.5 km in space and 10 min in time. The full CPOL archive runs from 1998 to 2017—with 2 years without operation—which is the period that was scanned to identify the November 2006 sequence of cases that are the focus of this study.

2.3 | Model set-up

The aforementioned convective storms are reproduced using the limited-area version of the UM with the Regional Atmosphere configuration for the Tropics (RA1-T; Bush *et al.*, 2019). In a recent study, Dipankar *et al.* (2020) observed forecasting improvements when utilising European Centre for Medium-Range Weather Forecasts analysis rather than UM Global Atmosphere (GA) data to drive a UM-based limited-area model set-up. Following

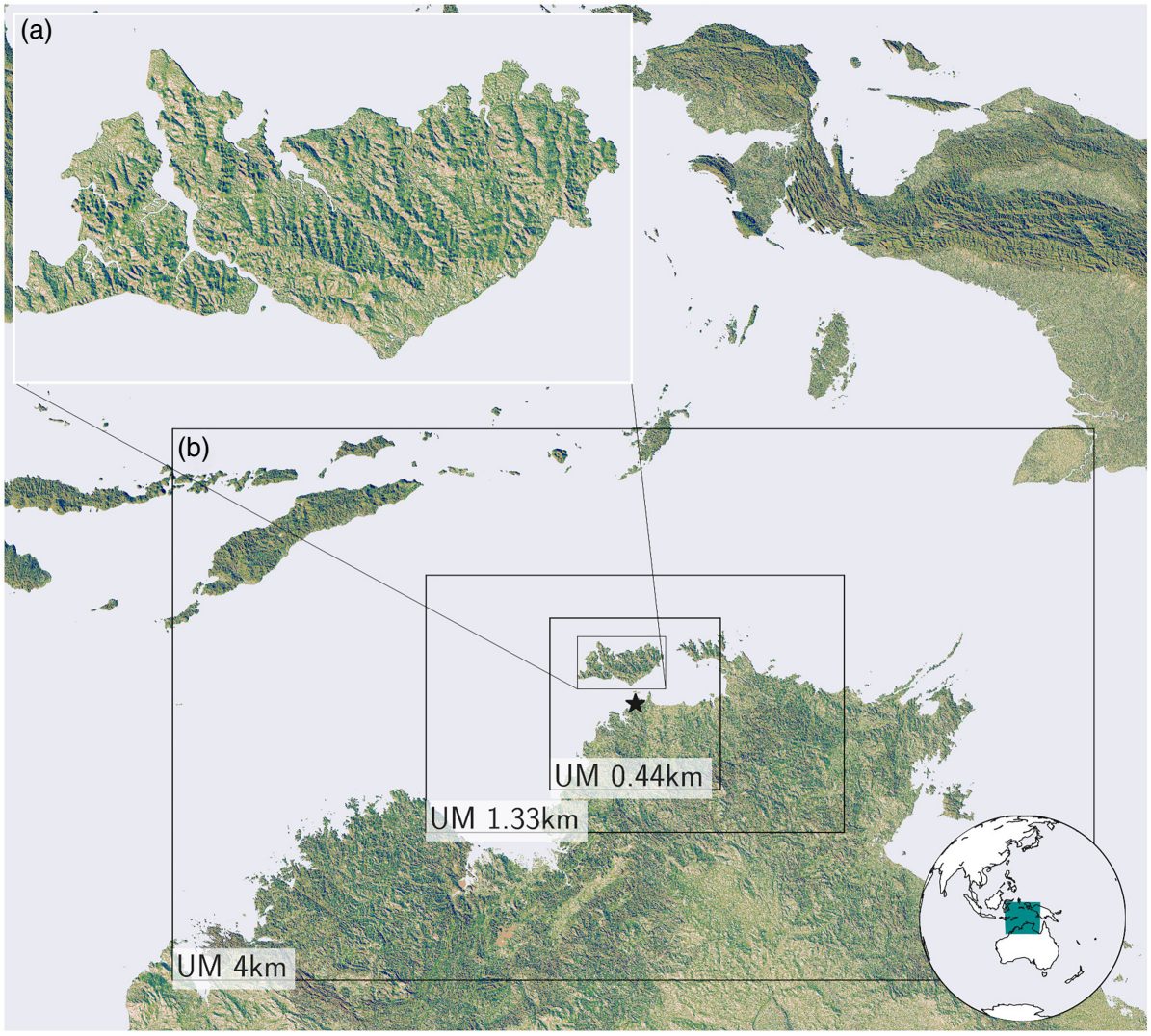

FIGURE 1 (a) The Tiwi Islands study domain. (b) The model domain boundaries of the triple nested set-up with their horizontal resolution. The location of the C-band dual-polarisation radar station is indicated by a black star [Colour figure can be viewed at wileyonlinelibrary.com]

this approach, we force our model set-up with the reanalysis ERA-Interim dataset (Berrisford *et al.*, 2011), which is made available at four daily times (0000 UTC, 0600 UTC, 1200 UTC, 1800 UTC) with a resolution of 0.7°. We apply three one-way nested domains at horizontal grid spacings of 4 km (UM 4km), 1.33 km (UM 1.33km), and 444 m (UM 0.44km) in the smallest domain (see also Figure 1b). The RA1-T science configuration was specifically developed for application in tropical areas, with 80 vertical levels and a model top of 38.5 km. Convection parametrisation is switched off in all simulations. RA1-T uses a prognostic large-scale cloud scheme (Wilson *et al.*, 2008). Sub-grid mixing is parametrised using a blend of the three-dimensional Smagorinsky mixing scheme and the more traditional eddy-covariance parametrisation (Boutle *et al.*, 2014). Microphysical processes are represented by the Wilson and Ballard (1999) bulk microphysics scheme with prognostic liquid and ice cloud, as well as prognostic graupel and rain. The 4 km set-up is not included in this study as it is mostly influenced by the global driving model and we wish to compare the model output at the resolution of the observational dataset. Therefore, we regrid the 1.33 km and 0.44 km model datasets to the 2.5 km resolution of the CPOL observations using first-order conservative regridding before conducting any of the analysis presented here.

2.3.1 | Ensemble simulations

To gain more robust statistics when investigating extreme events we create a lagged ensemble of eight members.

The ensemble is created by varying the initial times of the individual members. The sets of initial conditions are 6 hr apart with the first member being initiated 2006-11-08 1800 UTC and the last one at November 11, 2006, 0000 UTC. As already mentioned, the time period that is analysed in this study is November 11, 2006, 1200 UTC to November 19, 2006, 1200 UTC, allowing for at least 12 hr spin-up phase for each ensemble member. Each simulation (ensemble member) is then run for the entire period, while the boundaries of the 4 km domain are constrained by the ERA-I large-scale conditions. Although the simulations are long (more than 8 days), it will be shown that, because of the localised forcing of these events, later stages of the simulation still provide good representation of the timing of the storms. Moreover, the outermost boundaries of the 4 km domain are also constrained by the reanalysis, which constrains the large-scale conditions.

2.4 | Thunderstorm tracking

To investigate storm life cycles and their statistics of extreme events we track rainfall cells in observed and model data using the TINT (Fridlind *et al.*, 2019) storm tracking package. The cell tracks are retrieved using phase correlation between two consecutive time steps and application of the Hungarian maximum matching algorithm (Kuhn, 1955) to identify cells that are connected in time. We adopted the original package, which has been developed for radar data only, to be able to track model- and radar-based rainfall data alike. The algorithm assigns every identified storm cell a unique identifier (uid). The Hungarian matching algorithm decides whether a new uid (a new storm cell appears or splits from another system) or an existing uid is assigned (a storm cell from the previous time step). These unique identifiers allow for a connection of individual storm cells in time. Because each contiguous rainfall region that gets identified by the tracking algorithm is labelled with an identifier unique in space and time, we will refer to this region as a *storm*. This might also include rainfall areas that are not the result of deep convection and that would not necessarily be called a thunderstorm. For both the model and the radar, we apply a rain-rate threshold of 0.1 $mm \cdot hr^{-1}$ and choose a minimum storm size 4 px to identify storms. The threshold of 0.1 $mm \cdot hr^{-1}$ has been chosen because the vast majority of raining pixels have a higher rain rate than 0.1 $mm \cdot hr^{-1}$. As a consequence, a sensitivity analysis of the applied rainfall threshold showed no sensitivity to rain-rate thresholds below 0.1 $mm \cdot hr^{-1}$. The storm size threshold of 4 px was chosen to have at least two adjacent raining pixels, which avoids taking grid-point storms into account.

3 | RESULTS

Before investigating the results of the experiment we focus on the large-scale atmospheric conditions over the largest model domain (displayed in Figure 1b) during the time period considered (i.e., November 11–19, 2006). These large-scale conditions are taken from the ERA-Interim reanalysis dataset. Mid-tropospheric prevailing winds are easterly (Figure 2a) advecting only moderately moist air into the domain (Figure 2b). The mean vertical motion is downward in the mid-troposphere (Figure 2c), which along with the relatively dry profile, suppresses large-scale convection. These properties are characteristic of the monsoon build-up period described in Narsey *et al.* (2017).

3.1 | Domain and time averages

After confirming that atmospheric conditions are favourable for locally forced convection we investigate how well averages of rainfall are captured by the model. Figure 3 compares the field-averaged (Tiwi Island domain, Figure 1a) time series of simulated rainfall with observations from the CPOL radar. Most of the intense rainfall events during the afternoons are captured by both model simulations, UM 1.33km and UM 0.44km. Yet, the simulated events during the afternoons of November 13, 14, and 15 are considerably weaker than the observations suggest. Around noon of November 17 an early rainfall peak occurs in the observations that is not captured by both sets of simulations, though later that afternoon a second peak is represented well. Because of weaker or missed rainfall events, the average simulated rainfall is lower in both model simulations. Overall, there is a reasonably good agreement between the observations and simulations, with only some occasions where the model is too intense (e.g., November 12). There is reasonable agreement amongst the ensemble members; only towards the end of the simulation does the ensemble spread become noticeable, which is perhaps expected due to the longer lead time. The dashed lines of Figure 3 represent the intensity of the 80th percentile of the area-averaged rain rates and show a decreased intensity of strong events (>80th percentiles) in the sub-kilometre model simulations (0.44 km), but closer agreement between the 1.33 km model and the observations. The time series also reveals that the rainfall peaks in the model occur generally too early, except for the strong event in the afternoon of November 17. Despite some of the differences in storm intensity and the aforementioned missed event, the ensemble simulations produce a Hector storm every day. This means that there is a total of 64 Hector events simulated for each model resolution, which is a good sample

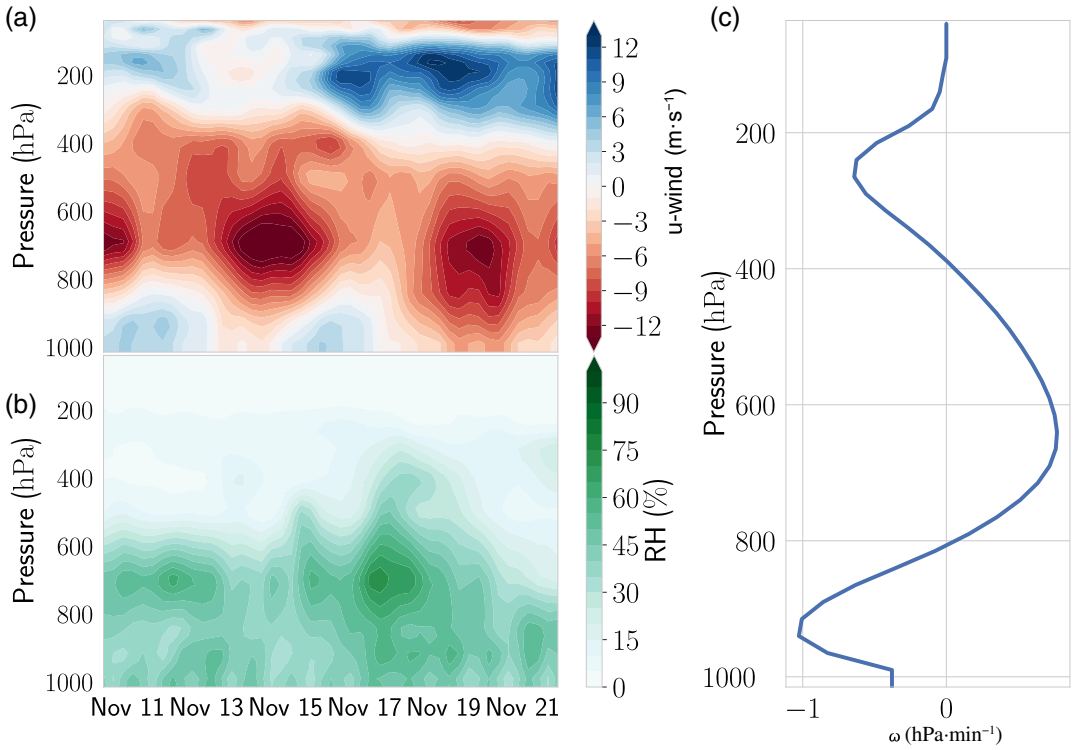

FIGURE 2 Large-scale atmospheric conditions between November 11 and November 19, 2006, over the largest model domain (Figure 1b): (a) *u*-component of horizontal winds; (b) relative humidity (RH); and (c) average vertical ω profile [Colour figure can be viewed at wileyonlinelibrary.com]

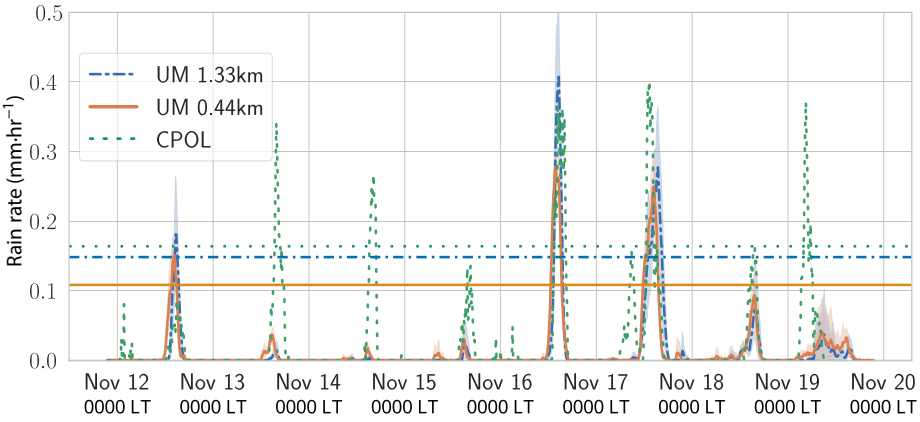

FIGURE 3 Rainfall: Domain averages of simulated ensemble means compared with observations. The individual ensemble members are indicated by the shading. Dashed lines indicate the 80th percentile of field-averaged rain rates. LT: local time (UTC + 9.5); CPOL: C-band dual-polarisation; UM: Unified Model [Colour figure can be viewed at wileyonlinelibrary.com]

size for comparison between resolutions and with the observations.

The interpretation of domain average rainfall can be misleading when the occurrence of those rainfall events is spatially isolated. We therefore compare maps of time averages shown in Figure 4. The maps reveal spatial rainfall biases. Though the observations suggest that rainfall is predominantly occurring over the south east—the smaller Bathurst Island—simulated rainfall occurs mainly over the centre of the large Melville Island. The ensemble standard deviation (centre row of Figure 4) shows maxima over Melville Island, indicating that most storms are confined to this area. As a consequence, the simulated rainfall only exceeds the rain rates of the observation in this area (bottom row of Figure 4). A slight decrease of rainfall bias in the sub-kilometre simulation compared with the kilometre version can be noticed, yet both simulations do, on average, underestimate the mean intensity of rainfall in the study domain.

An important aspect of simulating tropical convection is the right timing. Previous studies have suggested that convection-permitting models (including the UM) trigger convection too early, leading to biases in the diurnal rainfall cycle. We now investigate whether increasing to

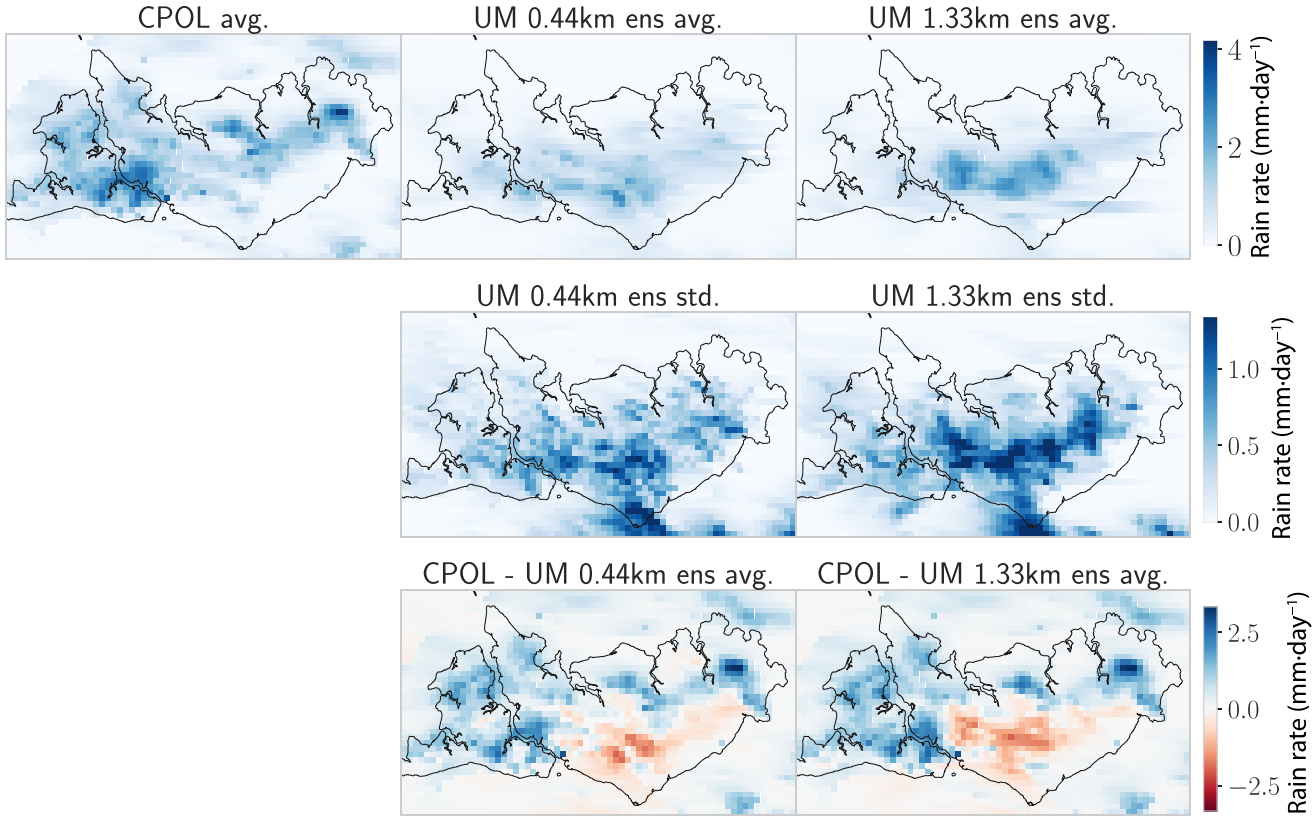

FIGURE 4 Maps of time-averaged rain rates (mm·day^{-1}). The top row shows the observations (C-band dual-polarisation [CPOL]) along with ensemble averages of the 0.44 and 1.33 km Unified Model (UM) simulations. The centre row represents the ensemble standard deviation of both model simulations, and the bottom row indicates the difference of the simulated ensemble mean and the observations [Colour figure can be viewed at wileyonlinelibrary.com]

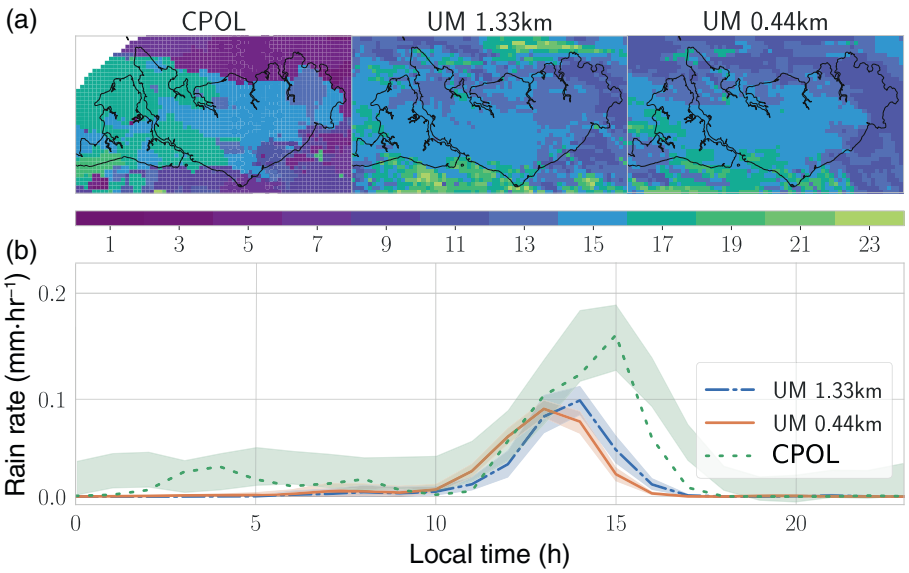

FIGURE 5 (a) Map of timing of daily rainfall peaks. (b) Domain average diurnal cycle. The shading around the C-band dual-polarisation (CPOL) data indicates the bounds of the 45th and 55th percentiles of rainfall occurring during all monsoon build-up periods. Local time is UTC + 9.5. UM: Unified Model [Colour figure can be viewed at wileyonlinelibrary.com]

sub-kilometre scales improves the representation of the diurnal cycle (Figure 5). For a comparison of how the observed diurnal cycle fits to all Monsoon build-up periods we also included the 45th and 55th percentiles of rainfall during all November monsoon build-up. Most notable is that in both simulations the ensemble average daily rainfall peak occurs roughly 2 hr earlier than the radar data peak. The early morning peak in the observations around 03:00 h–04:00 h (UTC + 9.5) is also not captured in either sets of the model simulations. The occurrence

timing of daily rainfall maximum per grid point is shown in Figure 5a. The bias in the timing of the peak rainfall is likely related to the fact that (after the early morning observed peak) the rainfall initiates about an hour early in both model domains—approximately 10:00 h local time (LT; UTC + 9.5) vs. 11:00 h LT (UTC + 9.5). Moreover, in the observations, the rainfall continues to increase in magnitude until 15:00 h LT (UTC + 9.5), potentially due to the development of stratiform rain, where the model rainfall decays earlier. The CPOL timing pattern suggests a propagation of storm systems from the north east of Melville Island across the centre of the island in the afternoon towards the south flank of Bathurst Island. This propagation is not fully captured by both models. Though there is some simulated propagation of convective systems from the north east of Melville Island towards the centre around local noon, the convection remains concentrated over the centre of the island. This is consistent with the spatial occurrence of rainfall in Figure 4, where most of the rainfall is located over the centre of Melville Island. It can be summarised that, on average, simulated rain rates are slightly underestimated compared with observations. Model rain is mainly focused over the centre of Melville Island, which differs from the observations where convection is propagating across both islands with peaks over Bathurst Island. Compared with the CPOL observational data, the simulated rainfall occurs too early. Some of these timing and magnitude errors may be related to a failure of the model to develop enough stratiform rain in the afternoon, a problem slightly more prevalent in the higher resolution model. These errors are consistent with the changes in storm characteristics identifies in the next section.

3.2 | Storm track analysis

Because the thunderstorms are isolated and the rainfall field is sparse in space and time, conclusions drawn from an average can be misleading. We now want to avoid averaging as much as possible and look at individual storms while preserving statistical robustness. We track individual storms in space and time using the tracking algorithm described in Section 2.4. The reader is reminded here that we call any contiguous rainfall area that gets picked up by the tracking algorithm a storm, regardless of its size or intensity. Here, the storm size is measured as an equivalent radius, which we calculate from the median storm area. The number of storms for the model simulations is the ensemble average. Table 1 summarises the median properties of the storms identified. We calculate the median's uncertainty ranges by bootstrapping the samples 10,000 times. The lower and upper bounds represent the 2.5th and the 97.5th percentiles of the bootstrapped median values. We also include all monsoon build-up periods in the CPOL bootstrapping procedure for a more robust observational sample size.

Most notable is the difference in storm size and number between model simulations and observations. The simulated storms are smaller in size but more numerous. The smallest and shortest-lived storms occur in the sub-kilometre model simulations. The UM 0.44km version also overestimates the storm intensities with an average rain rate per storm of 5.55 $mm \cdot hr^{-1}$. With 4.78 $mm \cdot hr^{-1}$ the UM 1.33km version only slightly overestimates the storm intensities, compared with its sub-kilometre counterpart. This is in contrast to the results shown in Section 3.1, where time- and domain-averaged rainfall is smaller in the simulations. This underestimation is most likely a result of a combination of decreased simulated storm areas (UM 1.33km) and shorter duration (UM 0.44km).

Although each model ensemble member was initialised with different conditions (see also Section 2.3), only towards the end of the simulation does an increasing ensemble spread become noticeable (see also Figure 3). Especially during the first day of the simulation, the storms

TABLE 1 Count and bootstrapped median properties of objectively tracked storms

	UM 0.44km	UM 1.33km	CPOL	CPOL all
# Storms	73 ± 4	50 ± 6	42	882
Median average rain rate ($mm \cdot hr^{-1}$)	5.55 [5.13, 5.91]	4.78 [4.35, 5.03]	4.50 [4.06, 4.76]	4.46 [3.84, 5.15]
Median maximum rain rate ($mm \cdot hr^{-1}$)	12.99 [11.98, 14.41]	12.31 [9.76, 15.27]	12.07 [9.64, 14.91]	12.32 [9.67, 15.26]
Median equivalent radius (km)	4.29 [4.05, 4.63]	4.90 [4.68, 5.25]	6.12 [5.62, 7.99]	5.59 [4.99, 6.34]
Median duration (min)	50.00 [40.0, 60.0]	60.00 [50.0, 65.0]	64.67 [50.13, 93.47]	59.07 [50.53, 69.73]
Median speed ($km \cdot hr^{-1}$)	12.39 [11.63, 13.09]	10.02 [9.62, 10.51]	12.78 [10.45, 15.87]	12.88 [11.48, 14.74]

Note: The storm count (# Storms) is given as an ensemble average and standard deviation for the simulated data (UM 1.33km and UM 0.44km). The uncertainty of the median values range represents the 2.5th and 97.5th percentiles for the bootstrapped median distribution. Observations for all November monsoon build-up periods (CPOL all) have been added for comparison. CPOL: C-band dual-polarisation.

TABLE 2 Differences of median values for tracking analysis taking the first day into account and without the first day

	UM 0.44km	UM 1.33km
Average rain rate (mm·hr^{-1})	−0.36%	0.00%
Maximum rain rate (mm·hr^{-1})	−0.46%	0.26%
Equivalent radius (km)	0.00%	−0.20%
Duration (min)	0.00%	0.00%
Speed (km·hr^{-1})	−0.23%	−0.20%

Note: The differences are displayed as a percentage of the median values taking the first day into account.

might be very similar among the ensemble member. To evaluate how independent these early simulated storms amongst the ensemble members are, we perform the storm tracking without the first day and compare the results with those taking the first day into account. Table 2 shows the differences between the median values given in Table 1 and their counterparts derived from the analysis without the first day. For a better comparison, we compute the differences as a percentage of the median values in Table 1. Overall, the influence of the first-day storms is only a fraction of a per cent, which means the results are not sensitive to potentially similar storms occurring early in the simulations.

We now want to investigate storm properties of more extreme events and group tracked storms by their average rainfall intensity. To cater for the different intensities in model simulations and observations we rank the storms by rain-rate quintile and compare the distributions of individual storm cell properties occurring during the storm lifetimes within each rank. Figure 6 shows distributions of the three storm cell properties rain rate, duration, and size (equivalent radius). To average as little as possible and to conserve a robust sample size when grouping the datasets, we choose to consider individual storm cells rather taking averages of storm properties across their life cycles for the variables rain rate and storm size. This approach cannot be applied for storm duration; therefore, we chose to create an observational ensemble by bootstrapping storm tracks of all November monsoon build-up periods defined by Narsey *et al.* (2017) during the entire CPOL era (1998–2017). This approach yields an observational dataset of 21 ensemble members with 42 storms per ensemble. To compare the week analysed with the rest of the November monsoon build-up period, we also include quintile distributions for all November periods (CPOL all) analysed.

The rain rates for both simulated and observed storms are increasing with quintile, as expected. They are considerably higher in the sub-kilometre model simulations than

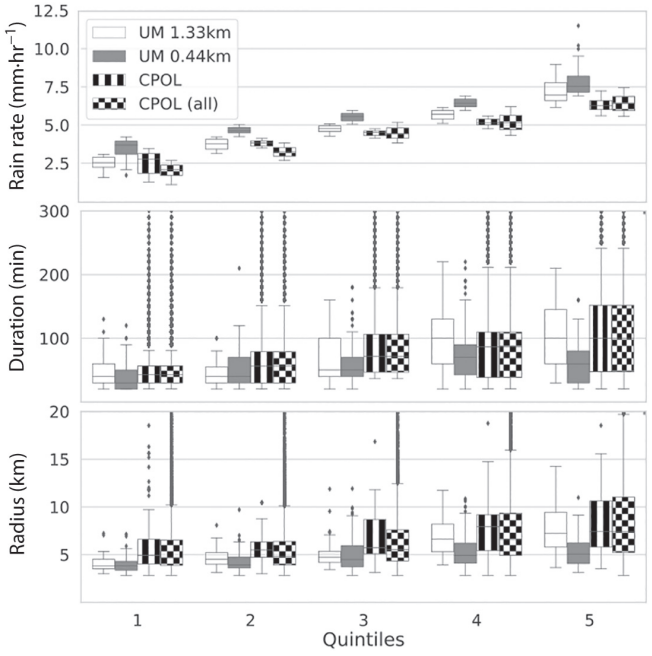

FIGURE 6 Storm track properties grouped by rain-rate intensities (quintiles). Observations for all November monsoon build-up periods (CPOL all) have been added for comparison. CPOL: C-band dual-polarisation

with its 1.33 km counterpart, which, in turn, are higher across all quintiles than the observations. With increasing quintile, the gap between observations and model simulations becomes larger. The pattern of storm duration and size with increasing rain intensity also reflects the results shown in Table 1. The sub-kilometre model storms have a shorter duration and a smaller size than 1.33 km model and the observed storms, too. It is interesting to note that there is only a moderate increase in storm duration with quintiles for simulations and observations alike. This is also the case for the storm sizes, except for the UM 1.33km model version, where a jump in duration can be observed between the third and fourth quintiles. This jump contributes to the decreased size bias of the UM 1.33km version shown in Table 1.

Figure 4 suggests that the majority of the simulated storms do develop and disappear over the centre of Melville Island, while propagation across both the Tiwi Islands is observed. This can easily be confirmed with the help of the storm track analysis. Figure 7 displays tracks for the most intense storms (fifth quintile). Most of the simulated tracks are concentrated over the centre of Melville Island. This is in stark contrast to the observed storm tracks, which are all propagating from east to west across the Tiwi Islands. The track length of simulated storms is also much shorter than for the observed storms. Although most of the simulated storms do propagate from east to

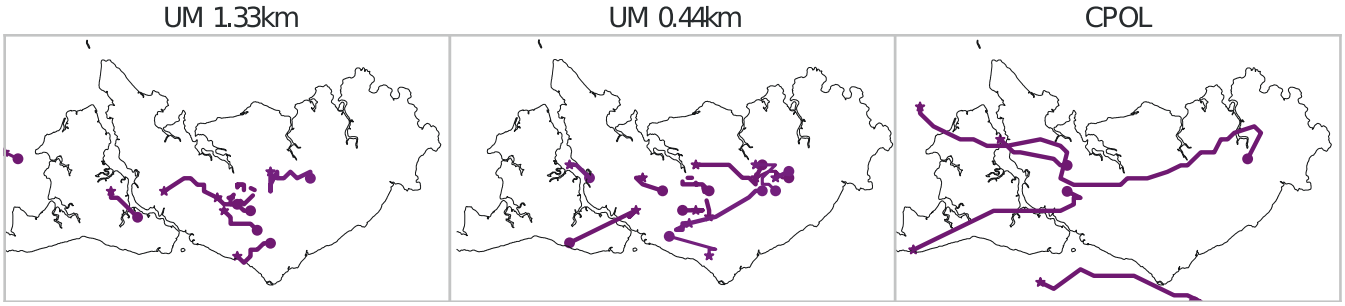

FIGURE 7 Storm tracks with intensities of the fifth quintile. For better readability we choose to only display the first ensemble member in both model simulations. CPOL: C-band dual-polarisation; •, start of storm track; ⋆, end point of storm track [Colour figure can be viewed at wileyonlinelibrary.com]

west (• indicates initiation of the storm and ⋆ its decay), some storms propagate in the opposite direction. As shown here for the most intense quintile, the sub-kilometre model version produces, overall, more numerous and shorter storms than the 1.33 km model does, which is also the case for the fourth quintile.

At this point it can be summarised that the simulated storms are smaller in size, more numerous, and more intense than the observed storms. Most of the intense storms are confined to a rather small area over the centre of Melville Island. This is contrast to the observations that show systems propagating across the Tiwi Islands. The increased number of storms and intensity cannot fully compensate for the effects of decreased size and lifetime in the case of the sub-kilometre model version. The detailed storm track investigation suggested that increasing the resolution to sub-kilometre scales does not necessarily lead to a better representation of storms, and by some measures the characteristics of the more intense storms are worse.

3.3 | Convection and cold-pool properties

We now want to answer the question of why the sub-kilometre model version is performing poorer than its kilometre-scale counterpart and investigate atmospheric conditions in which the simulated storms occur. Because we do not have adequate observations of the mesoscale structure of the atmosphere, this section only considers the two model versions and not the observations.

Making statements about simulated atmospheric conditions that are associated with thunderstorms is somewhat tricky. One approach might be taking snapshots of the storm and investigate profiles of certain variables like vertical motion or moisture flux. We do not choose to take this approach as we want to take all simulated storms into account, which allows for a more robust investigation of extreme events. Instead, we take the storms tracks and examine various atmospheric variables within individual storms along their trajectory. For simplicity, we take the storm cell size s_{i_t} of a storm U_{i_t} at time t and estimate the vertical profile of the atmosphere within a square of size s_{i_t} at time t around the centre of U_{i_t}. This technique allows us to retrieve profiles for all individual storms cells in the dataset and to discriminate against storm cells with different intensities.

One important indicator of convection is the profile of vertical motion anomalies $\overline{w'} = \langle w - \overline{w} \rangle$, where $\overline{w}$ is computed from the domain-averaged vertical velocity at a given model level. Figure 8a shows the average profile of vertical motion grouped by storm intensity. Overall, a strong increase in mean updraft strength with storm intensity can be noticed. This is as expected, since the storms considered are of convective nature and there is a close association between rain rate (used to define the quintiles) and updraft strength. The less intense storms, within the first and second quintiles, are associated with vertical motion that is peaking in the lower troposphere, which indicates that the associated convection is not deep and is mainly in the boundary layer or congestus. The more intense storms are not surprisingly associated with vertical motion profiles found in deeper convective system where an intensification of vertical motion in the mid-troposphere can be observed. The differences of the two profiles for the 1.33 km and 0.44 km models is noteworthy. This is especially true of the upper quintile, where the 1.33 km and 0.44 km models possess different shapes to the profile; the 1.33 km model has a peak in the upper troposphere. Figure 8b displays the average profiles of turbulent moisture flux, which are closely linked to the vertical motion profiles. Peaks over vertical moisture fluxes occur in the upper to mid-troposphere (600–400 hPa) for the highest percentiles. The differences of the flux and vertical moisture profiles between the two model simulations are consistent with the behaviour of rainfall in Figure 6. For the upper three quintiles, the 1.33 km model shows fluxes extending deeper than the 0.44 km model. Such

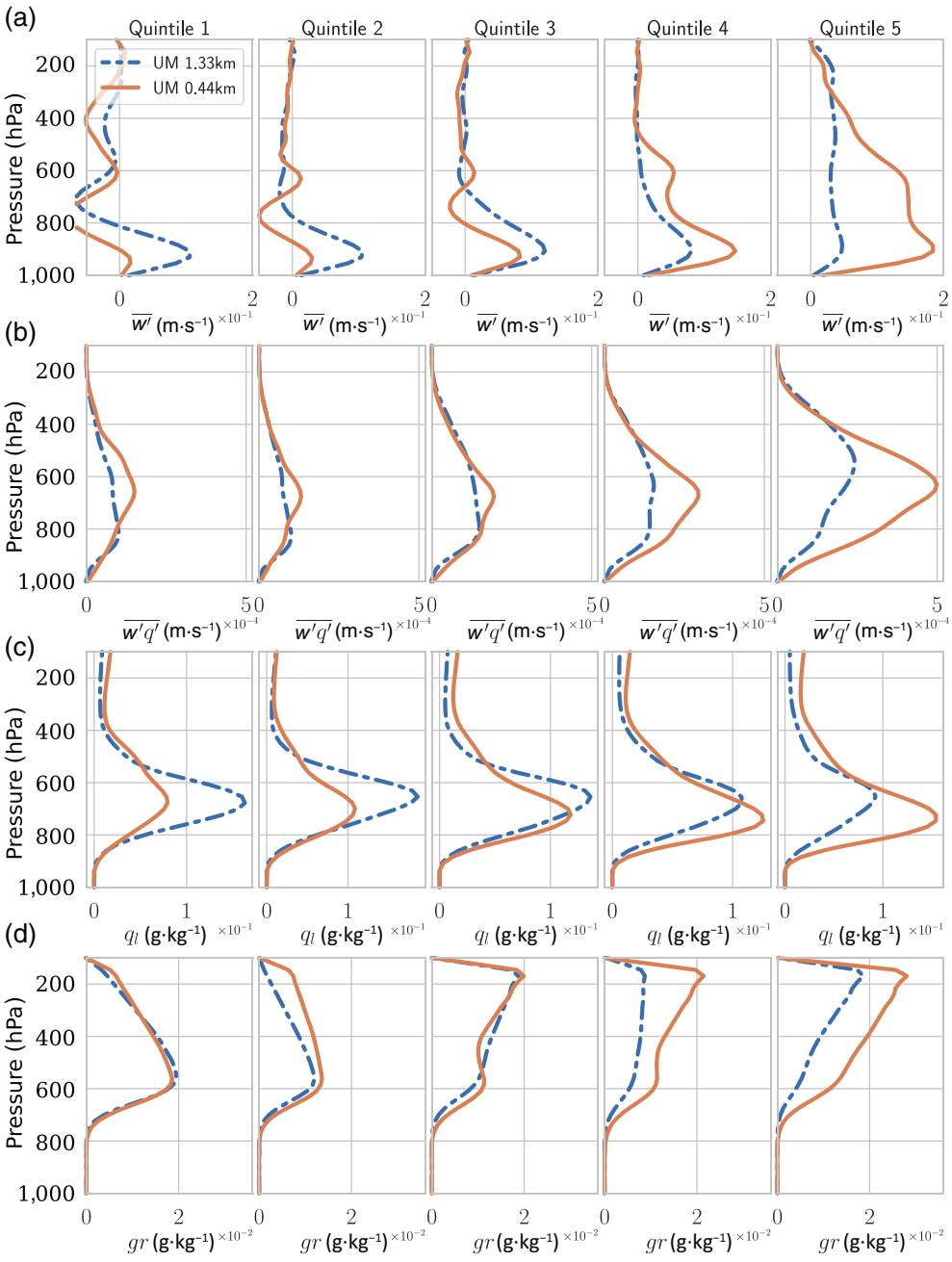

FIGURE 8 Average vertical profiles of (a) vertical motion fluctuations, (b) vertical moisture flux fluctuation, (c) cloud liquid water content, and (d) graupel concentration (gr) grouped by storm intensity. The storm intensities are based on rain-rate quintiles [Colour figure can be viewed at wileyonlinelibrary.com]

deeper updraft effects would be consistent with reduced entrainment in the coarser model, as suggested by Bryan *et al.* (2003). The fluxes are, however, stronger in the higher resolution model (for the upper two quintiles); conferring with Figure 6b, this suggests that as the storms are more intense they must become shorter-lived. These results have some consistency with Jucker *et al.* (2020), who showed a strengthening of the kinetic energy spectrum for the smallest resolvable scales. Such a strengthening would lead to the smaller, stronger storm cells shown here, suggesting ineffective mixing and a dominance of numerical effects on these scales. An important model component that can modify the characteristics of convection, and subsequently rainfall, is the cloud microphysics. To consider this, the average liquid water and graupel content per storm is displayed in Figure 8d. The profiles of liquid water content q_l follow a similar pattern to the vertical velocity, with the 1.33 km model being stronger at lower quintiles and the 0.44 km model being stronger at upper quintiles. For the graupel, however, it is only the fourth and fifth quintiles that show the large increase in graupel in the 0.44 km model. These results suggest that the strongest storms in the 0.44 km model are much more effective in transporting moisture to the upper

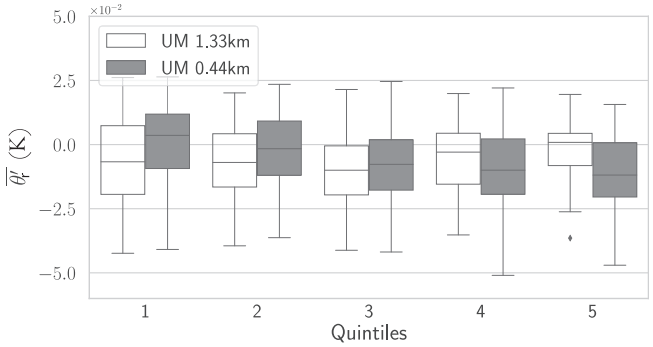

FIGURE 9 Distribution of field perturbations of density potential temperature. UM: Unified Model

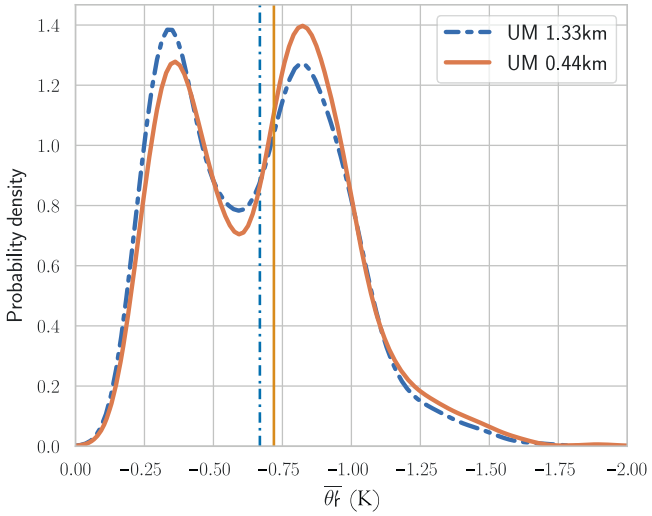

FIGURE 10 Comparison of the probability density of cold-pool strength, indicated by the field perturbation of density potential temperature ($\overline{\theta'_\rho}$). The medians are shown by the dashed lines. UM: Unified Model [Colour figure can be viewed at wileyonlinelibrary.com]

troposphere, with the formation of graupel being one consequence. These changes in microphysical properties between the 1.33 and 0.44 km model storms likely have important feedbacks on rainfall, evaporation, and other storm properties.

As mentioned in Section 1, owing to the topographic set-up of the Tiwi Islands, thunderstorm events can intensify by interaction of sea-breeze convergence lines and outflows from the convective systems. This suggests that the boundary layer can play an important role for the intensification of the storms, especially via cold pools. To find any relationships of the tracked storms and cold-pool fields we first calculate the perturbations of surface density potential temperature θ_ρ. Here, we follow the approach of Tompkins (2001) and define θ_ρ at the surface as

$$\theta_\rho = \theta \cdot (1 + 0.608 \cdot r_v - r_r), \tag{1}$$

with θ being the potential temperature and r_v and r_r being the mixing ratios for water vapour and rain respectively. We follow the procedure mentioned earlier and retrieve the perturbation field of θ_ρ for each identified storm and group the $\overline{\theta'_\rho}$ values by storm intensity (Figure 9a).

Overall, there is only a weak θ_ρ decrease with storm intensity (which is more discernible for the sub-kilometre version) to be recognised. For the weak storms, the medians of the distributions are positive or only slightly negative, which indicates either absences of or very moderate density perturbations. With increasing storm intensity the θ_ρ perturbation for the sub-kilometre model decreases slightly. The inter-model comparison suggests that there might be a small intensification of cold-pool activity in the sub-kilometre-scale model, for quintiles 4 and 5, consistent with the stronger rain rates seen earlier.

3.3.1 | Tracking cold pools with help of the θ_ρ perturbation field

The aforementioned comparison of density potential temperature, as a function of storm intensity, does not show a clear signal. To gain deeper insights on cold-pool strength in the two simulations we utilise the perturbation fields of θ_ρ and apply a threshold of 0 K to track cold pools using the tracking algorithm introduced earlier herein. We do not choose to compare the cold-pool tracks with the storm tracking results here as matching storms tracks to cold pool tracks has many ambiguities, especially in regions with multiple storms and cold pools. Figure 10 compares the probability density functions of tracked cold pools, represented by θ_ρ anomalies, for the two model simulations. The two distributions show a clear bimodal behaviour, where the second mode that is associated with stronger cold pools has higher densities in the sub-kilometre ensemble simulations. As a consequence, the cold pools in the 0.44 km models are −0.71 K on average (13.15%), stronger than in the 1.33 km version (−0.66 K); as discussed earlier, stronger cold pools are consistent with the more intense rain for the 0.44 km model.

4 | SUMMARY AND DISCUSSION

This study investigated the representation of intense convective rainfall events in a set of simulations using kilometre- and sub-kilometre-scale grid spacings. We

focused on the simulation of a sequence of island thunderstorm events over the Tiwi Islands in northern Australia during the build-up period of the Australian summer monsoon in November 2006. We chose the build-up period as the convection is mainly locally forced (see also Figure 2), which reduces (but does not eliminate) the effect of the global input model and variations in the larger scale forcing. The model set-up uses ERA-Interim reanalysis data as initial and boundary conditions for a nested set-up with horizontal grid spacings equal to 4, 1.33, and 0.44 km. Our particular focus was on the more intense events within the two finest grids with grid spacing equal to 1.33 and 0.44 km. To increase the sample size, which can be low for intense events, we chose to create an ensemble of eight members; with our focus on an 8-day period, the model ensemble therefore produced 64 daily storm events (i.e., Hectors).

Applying spatial and temporal averaging suggested that both model resolutions underestimate the rain rates when compared with observations. This is in part due to three strong rainfall events that are missed by the model simulations (Figure 3). The geospatial distribution of rainfall (Figure 4) showed that simulated rainfall is concentrated over the centre of the Tiwi Island's main island, whereas rainfall peaks in the observations mainly occur in the east and west of the domain. An investigation of the timing of convection confirmed the results of other studies using high-resolution simulation: on average, the simulated rainfall peak occurs too early. Increasing the resolution slightly worsened the rainfall timing. By only considering spatio-temporal averages of rainfall fields it can be summarised that the intensity of island thunderstorm events is underestimated by the model and that increasing the resolution to sub-kilometre scales does not significantly improve their representation (Figure 3). Although the errors in timing are consistent with recent studies of convection in the Maritime Continent using convection-permitting models (e.g., Vincent and Lane, 2017; Jucker *et al.*, 2020), the errors in amplitude are different. The main difference between Jucker *et al.* (2020), who showed the modelled rainfall over the mainland to be too intense, and the results herein is that the convection over the islands here does not become organised and is mostly comprised of short-lived cells. The reasons for these differences should be a topic of future research.

To get more meaningful insights of single events while retaining statistical robustness, we tracked observed and simulated storm events in space and time by objectively identifying storm objects. This allowed us to discriminate storm properties like size and duration against storm intensities. This comparison showed that simulated thunderstorm events are, in general, more numerous, smaller, and intense. The underestimation of area/time-averaged rain rates is hence the result of a combination of smaller, slightly shorter-lived, and more intense storms (Figure 6) that are focused over a comparable small area. It is noteworthy that increasing the resolution worsens this effect: storms in the sub-kilometre model are even shorter lived, smaller, and more intense than observed, especially for the strongest storms. This result is in contrast to some previous studies, which suggest that at sub-kilometre scales the increase in resolved entrainment should weaken updrafts (Bryan *et al.*, 2003). However, the result is consistent with the tendency for this specific model to have enhanced kinetic energy at the smallest resolvable scales (Jucker *et al.*, 2020), which leads to intense and small updrafts. A clear increase of mid-tropospheric turbulent vertical velocity and moisture flux in the sub-kilometre model is the reason for this intensification of storms. The comparison of graupel content exhibits decreased graupel contents in the sub-kilometre version, likely related to the smaller and shorter-lived storms.

We also examined any changes in cold-pool intensity with resolution by applying the aforementioned tracking algorithm to perturbation fields of density potential temperature. The results of this tracking do confirm that cold pools in the sub-kilometre models are more intense. This increased cold-pool intensity may be a result of the stronger rainfall in the sub-kilometre model, but may also contribute to an increase in rainfall intensity.

The question of cold-pool activity is also very important to answer, as previous studies suggested that an interaction of sea-breeze fronts and cold air outflow from developing convection play an important role in the intensification and formation of extreme island thunderstorm systems. A feedback sequence of how simulated storms intensify could be described as follows:

1. Low-level sea-breeze convergence causes occurrence of convection that is focused on a rather small area.
2. This convection also causes water vapour to transform to liquid water, which is then being transformed into ice, snow, and graupel in the upper part of the simulated cloud.
3. Evaporation of associated rain fluxes creates/intensifies the cold pool in the boundary layer below the clouds.
4. Cold pools produce stronger convergence by interaction with the sea-breeze fronts and/or cold air outflow from neighbouring clouds.

According to the aforementioned sequence, shortcomings in the microphysics parametrisation could cause feedback loops, with more intense updrafts as a result. This final point highlights the importance of physical parametrisations, such as microphysics and turbulence, and their role

in contributing to resolution sensitivities. Complex numerical weather prediction style models, such as the UM, make disentangling the causes of resolution sensitivity challenging, and changes to one scheme have downstream influences on others. To fully test the possible mechanism outlined, we suggest that future studies should aim to investigate the impact of physical parametrisations, especially at sub-kilometre scales, with simpler model frameworks. We recognise that there are many such idealised studies in the literature already, but it appears that some of these resolution sensitivities are model specific (e.g., Jucker *et al.*, 2020), making such idealised studies with the UM necessary. Emphasis should be given to tuning parameters that have to be set manually—deep-learning algorithms are well suited for optimising large sets of tuning parameters. Investigating the capabilities of such machine-learning tools might be a step towards significant improvements of remaining parametrisations in high-resolution numerical weather prediction and climate models.

AUTHOR CONTRIBUTIONS

Martin Bergemann: conceptualization; formal analysis; investigation; methodology; software; visualization; writing – original draft. **Todd P. Lane:** funding acquisition; project administration; resources; supervision. **Scott Wales:** software; writing – review and editing. **Sugata Narsey:** writing – review and editing. **Valentin Louf:** data curation; writing – review and editing.

ACKNOWLEDGMENT

This work was funded by the Australian Research Council's (ARC) Centre of Excellence for Climate Extremes (CLEX; grant number: CE170100023) Observations from the CPOL Doppler radar have been made available by the Bureau of Meteorology. The tracking algorithm is published under MIT open-source license and can be retrieved at https://zenodo.org/record/7051229. Computing facilities were provided by the National Computational Infrastructure (NCI) facility in Canberra, Australia. Thank you to Stuart Webster, UK Met Office, for assistance with the model. Finally, we would like to thank two anonymous reviewers whose suggestions significantly improved the quality of this article. Open access publishing facilitated by The University of Melbourne, as part of the Wiley - The University of Melbourne agreement via the Council of Australian University Librarians.

ORCID

Martin Bergemann https://orcid.org/0000-0003-0604-4103

REFERENCES

Bergemann, M. and Jakob, C. (2016) How important is tropospheric humidity for coastal rainfall in the tropics? *Geophysical Research Letters*, 43(19), 5860–5868.

Bergemann, M., Jakob, C. and Lane, T.P. (2015) Global detection and analysis of coastline-associated rainfall using an objective pattern recognition technique. *Journal of Climate*, 28(18), 7225–7236.

Beringer, J., Tapper, N.J. and Keenan, T.D. (2001) Evolution of maritime continent thunderstorms under varying meteorological conditions over the Tiwi islands. *International Journal of Climatology*, 21(8), 1021–1036.

Berrisford, P., Dee, D., Poli, P., Brugge, R., Fielding, M., Fuentes, M., Kållberg, P., Kobayashi, S., Uppala, S. and Simmons, A. (2011) *The Era-Interim Archive Version 2.0*. ECMWF. Technical report.

Birch, C.E., Webster, S., Peatman, S.C., Parker, D.J., Matthews, A.J., Li, Y. and Hassim, M.E.E. (2016) Scale interactions between the MJO and the western Maritime Continent. *Journal of Climate*, 29(7), 2471–2492.

Boutle, I.A., Eyre, J.E.J. and Lock, A.P. (2014) Seamless stratocumulus simulation across the turbulent gray zone. *Monthly Weather Review*, 142(4), 1655–1668.

Bryan, G.H., Wyngaard, J.C. and Fritsch, J.M. (2003) Resolution requirements for the simulation of deep moist convection. *Monthly Weather Review*, 131(10), 2394–2416.

Bush, M., Allen, T., Bain, C., Boutle, I., Edwards, J., Finnenkoetter, A., Franklin, C., Hanley, K., Lean, H., Lock, A., Manners, J., Mittermaier, M., Morcrette, C., North, R., Petch, J., Short, C., Vosper, S., Walters, D., Webster, S., Weeks, M., Wilkinson, J., Wood, N. and Zerroukat, M. (2019) The first Met Office unified model/JULES regional atmosphere and land configuration, RAL1. *Geoscientific Model Development – Discussions*, 13(4), 1999–2029.

Chan, S.C., Kendon, E.J., Fowler, H.J., Blenkinsop, S., Ferro, C.A.T. and Stephenson, D.B. (2013) Does increasing the spatial resolution of a regional climate model improve the simulated daily precipitation? *Climate Dynamics*, 41(5), 1475–1495.

Chan, S.C., Kendon, E.J., Fowler, H.J., Blenkinsop, S., Roberts, N.M. and Ferro, C.A.T. (2014) The value of high-resolution met office regional climate models in the simulation of multihourly precipitation extremes. *Journal of Climate*, 27(16), 6155–6174.

Crook, N.A. (2001) Understanding Hector: the dynamics of island thunderstorms. *Monthly Weather Review*, 129(6), 1550–1563.

Dauhut, T., Chaboureau, J.-P., Escobar, J. and Mascart, P. (2016) Giga-LES of Hector the Convector and its two tallest updrafts up to the stratosphere. *Journal of the Atmospheric Sciences*, 73(12), 5041–5060.

Dauhut, T., Chaboureau, J.-P., Mascart, P. and Pauluis, O. (2017) The atmospheric overturning induced by Hector the Convector. *Journal of the Atmospheric Sciences*, 74(10), 3271–3284.

Dipankar, A., Webster, S., Sun, X., Sanchez, C., North, R., Furtado, K., Wilkinson, J., Lock, A., Vosper, S., Huang, X.-Y. and Barker, D. (2020) Singv: a convective-scale weather forecast model for Singapore. *Quarterly Journal of the Royal Meteorological Society*, 146(733), 4131–4146.

Fridlind, A.M., van Lier-Walqui, M., Collis, S., Giangrande, S.E., Jackson, R.C., Li, X., Matsui, T., Orville, R., Picel, M.H., Rosenfeld, D., Ryzhkov, A., Weitz, R. and Zhang, P. (2019) Use of polarimetric radar measurements to constrain simulated convective cell evolution: a pilot study with lagrangian tracking. *Atmospheric Measurement Techniques*, 12(6), 2979–3000.

Gevorgyan, A. (2018) Convection-permitting simulation of a heavy rainfall event in Armenia using the WRF model. *Journal of Geophysical Research – Atmospheres*, 123(19), 11008–11029.

Gianotti, R.L., Zhang, D. and Eltahir, E.A.B. (2011) Assessment of the regional climate model version 3 over the maritime continent using different cumulus parameterization and land surface schemes. *Journal of Climate*, 25(2), 638–656.

Gill, A.E. (1980) Some simple solutions for heat-induced tropical circulation. *Quarterly Journal of the Royal Meteorological Society*, 106(449), 447–462.

Hassim, M.E.E., Lane, T.P. and Grabowski, W.W. (2016) The diurnal cycle of rainfall over new Guinea in convection-permitting WRF simulations. *Atmospheric Chemistry and Physics*, 16(1), 161–175.

Jucker, M., Lane, T.P., Vincent, C.L., Webster, S., Wales, S.A. and Louf, V. (2020) Locally forced convection in subkilometre-scale simulations with the unified model and WRF. *Quarterly Journal of the Royal Meteorological Society*, 146(732), 3450–3465.

Keat, W.J., Stein, T.H.M., Phaduli, E., Landman, S., Becker, E., Bopape, M.-J.M., Hanley, K.E., Lean, H.W. and Webster, S. (2019) Convective initiation and storm life cycles in convection-permitting simulations of the met office unified model over South Africa. *Quarterly Journal of the Royal Meteorological Society*, 145(721), 1323–1336.

Keenan, T., Glasson, K., Cummings, F., Bird, T.S., Keeler, J. and Lutz, J. (1998) The BMRC/NCAR C-band polarimetric (C-Pol) radar system. *Journal of Atmospheric and Oceanic Technology*, 15(4), 871–886.

Keenan, T., Rutledge, S., Carbone, R., Wilson, J., Takahashi, T., May, P., Tapper, N., Platt, M., Hacker, J., Sekelsky, S., Moncrieff, M., Saito, K., Holland, G., Crook, A. and Gage, K. (2000) The Maritime Continent – Thunderstorm Experiment (MCTEX): overview and some results. *Bulletin of the American Meteorological Society*, 81(10), 2433–2456.

Keenan, T.D., Morton, B.R., Manton, M.J. and Holland, G.J. (1989) The Island Thunderstorm Experiment (ITEX) – a study of tropical thunderstorms in the maritime continent. *Bulletin of the American Meteorological Society*, 70(2), 152–159.

Kuhn, H.W. (1955) The Hungarian method for the assignment problem. *Naval Research Logistics Quarterly*, 2(1–2), 83–97.

Leroy, D., Coutris, P., Emmanuel, F., Schwarzenboeck, A., Strapp, J.W., Lilie, L.E., Korolev, A., McFarquhar, G., Dezitter, F. and Grandin, A. (2016) HAIC/HIWC field campaigns – specific findings on ice crystals characteristics in high ice water content cloud regions. In: *AIAA AVIATION Forum*. American Institute of Aeronautics and Astronautics.

Louf, V., Protat, A., Warren, R.A., Collis, S.M., Wolff, D.B., Raunyiar, S., Jakob, C. and Petersen, W.A. (2018) An integrated approach to weather radar calibration and monitoring using ground clutter and satellite comparisons. *Journal of Atmospheric and Oceanic Technology*, 36(1), 17–39.

Love, B.S., Matthews, A.J. and Lister, G.M.S. (2011) The diurnal cycle of precipitation over the maritime continent in a high-resolution atmospheric model. *Quarterly Journal of the Royal Meteorological Society*, 137(657), 934–947.

Matsuno, T. (1966) Quasi-geostrophic motions in the equatorial area. *Journal of the Meteorological Society of Japan*, 44(1), 25–43.

May, P.T., Mather, J.H., Vaughan, G., Jakob, C., McFarquhar, G.M., Bower, K.N. and Mace, G.G. (2008) The tropical warm pool international cloud experiment. *Bulletin of the American Meteorological Society*, 89(5), 629–646.

Mori, S., Jun-Ichi, H., Tauhid, Y.I., Yamanaka, M.D., Okamoto, N., Murata, F., Sakurai, N., Hashiguchi, H. and Sribimawati, T. (2004) Diurnal land-sea rainfall peak migration over Sumatera Island, Indonesian Maritime Continent, observed by TRMM satellite and intensive rawinsonde soundings. *Monthly Weather Review*, 132(8), 2021–2039.

Narsey, S., Reeder, M.J., Ackerley, D. and Jakob, C. (2017) A midlatitude influence on Australian monsoon bursts. *Journal of Climate*, 30(14), 5377–5393.

Qian, J.-H. (2008) Why precipitation is mostly concentrated over islands in the Maritime Continent. *Journal of the Atmospheric Sciences*, 65(4), 1428–1441.

Ramage, C.S. (1968) Role of a tropical "maritime continent" in the atmospheric circulation. *Monthly Weather Review*, 96(6), 365–370.

Saito, K., Keenan, T., Holland, G. and Puri, K. (2001) Numerical simulation of the diurnal evolution of tropical island convection over the Maritime Continent. *Monthly Weather Review*, 129(3), 378–400.

Schafer, R., May, P.T., Keenan, T.D., McGuffie, K., Ecklund, W.L., Johnston, P.E. and Gage, K.S. (2001) Boundary layer development over a tropical island during the maritime continent thunderstorm experiment. *Journal of the Atmospheric Sciences*, 58(15), 2163–2179.

Simpson, J., Keenan, T., Ferrier, B., Simpson, R. and Holland, G. (1993) Cumulus mergers in the maritime continent region. *Meteorology and Atmospheric Physics*, 51(1–2), 73–99.

Simpson, J., Westcott, N., Clerman, R. and Pielke, R. (1980) On cumulus mergers. *Archiv für Meteorologie, Geophysik und Bioklimatologie, Serie A*, 29(1–2), 1–40.

Thompson, E.J., Rutledge, S.A., Dolan, B., Thurai, M. and Chandrasekar, V. (2017) Dual-polarization radar rainfall estimation over tropical oceans. *Journal of Applied Meteorology and Climatology*, 57(3), 755–775.

Tompkins, A.M. (2001) Organization of tropical convection in low vertical wind shears: the role of cold pools. *Journal of the Atmospheric Sciences*, 58(13), 1650–1672.

Trenberth, K.E., Fasullo, J.T. and Kiehl, J. (2009) Earth's global energy budget. *Bulletin of the American Meteorological Society*, 90(3), 311–324.

Vaughan, G., Schiller, C., MacKenzie, A.R., Bower, K., Peter, T., Schlager, H., Harris, N.R.P. and May, P.T. (2008) SCOUT-O3/ACTIVE: high-altitude aircraft measurements around deep tropical convection. *Bulletin of the American Meteorological Society*, 89(5), 647–662.

Vincent, C.L. and Lane, T.P. (2017) A 10-year austral summer climatology of observed and modeled intraseasonal, mesoscale, and diurnal variations over the maritime continent. *Journal of Climate*, 30(10), 3807–3828.

Wilson, D.R. and Ballard, S.P. (1999) A microphysically based precipitation scheme for the UK meteorological office unified model. *Quarterly Journal of the Royal Meteorological Society*, 125(557), 1607–1636.

Wilson, D.R., Bushell, A.C., Kerr-Munslow, A.M., Price, J.D. and Morcrette, C.J. (2008) PC2: a prognostic cloud fraction and condensation scheme. I: scheme description. *Quarterly Journal of the Royal Meteorological Society*, 134(637), 2093–2107.

Yamanaka, M.D., Ogino, S.-Y., Wu, P.-M., Jun-Ichi, H., Mori, S., Matsumoto, J. and Syamsudin, F. (2018) Maritime continent coastlines controlling Earth's climate. *Progress in Earth and Planetary Science*, 5(1), 21.

Zhu, M., Connolly, P., Vaughan, G., Choularton, T. and May, P.T. (2012) Numerical simulation of tropical island thunderstorms (Hectors) during the active campaign. *Meteorological Applications*, 20(3), 357–370.

How to cite this article: Bergemann, M., Lane, T.P., Wales, S., Narsey, S. & Louf, V. (2022) High-resolution simulations of tropical island thunderstorms: Does an increase in resolution improve the representation of extreme rainfall?. *Quarterly Journal of the Royal Meteorological Society*, 1–16. Available from: https://doi.org/10.1002/qj.4360